Geophysical Research Letters

RESEARCH LETTER
10.1029/2018GL081781

Special Section:
New Understanding of the Arabian Sea Circulation

Evolution of the Great Whirl Using an Altimetry-Based Eddy Tracking Algorithm

B.A. Melzer[1], T.G. Jensen[2], and A.V. Rydbeck[2]

[1]Perspecta, Stennis Space Center, MS, USA, [2]Naval Research Laboratory, Stennis Space Center, MS, USA

Key Points:
- A novel eddy identification and tracking algorithm tailored to the Great Whirl is developed
- Analysis of temporal evolution of the Great Whirl reveals a persistence well into the Northeast Monsoon
- Approximately 35% of the eddy kinetic energy within the Great Whirl is attributed to ageostrophic flow

Supporting Information:
- Supporting Information S1

Correspondence to:
B. A. Melzer,
bryce.melzer.ctr@nrlssc.navy.mil

Citation:
Melzer, B. A., Jensen, T. G., & Rydbeck, A. V. (2019). Evolution of the Great Whirl using an altimetry-based eddy tracking algorithm. *Geophysical Research Letters*, *46*, 4378–4385. https://doi.org/10.1029/2018GL081781

Received 20 DEC 2018
Accepted 14 MAR 2019
Published online 30 APR 2019

Abstract Twenty-three years of Archiving, Validation, and Interpretation of Satellite Oceanographic data absolute dynamic topography and HYbrid Coordinate Ocean Model sea surface height were analyzed with a focus on interannual variability of the Indian Southwest Monsoon in the southwest Arabian Sea. A new algorithm for identification and tracking of the Great Whirl (GW) is presented, which better accounts for the gyre's embedded environment than traditional mesoscale eddy tracking algorithms that use sea level observations. Based on this algorithm, the GW exhibits an average life span of 198 days, which is considerably longer than previous estimates, attributed primarily to a later termination date. A climatology of the GW evolution is created, peaking in early September. This study suggests a possible periodicity of the upper ocean structure during the mature phase of the GW and also highlights the sporadic nature of the decay phase.

Plain Language Summary The Great Whirl is an oceanic vortex that spins in a clockwise direction off the coast of east Africa. This feature is present for approximately half the year in coincidence with the Indian Southwest Monsoon. The Great Whirl is important because it can inhibit the flow of relatively fresh water into the salty Arabian Sea by recirculating the coastal current waters in a loop of intense currents. Here we evaluate a new algorithm specifically designed to track the Great Whirl. The algorithm is shown to provide increased accuracy in both satellite and model data over previous tracking methods and suggests a high-frequency periodicity in the size and strength of the Great Whirl, which has not yet been well documented. Additionally, interannual variability of the life cycle reveals a later termination date than previously thought.

1. Introduction

With the onset of the Indian Southwest Monsoon (ISM) during early May, the Somali Current system flows northward and is characterized by a retroflection into the interior of the Somali basin around 3°N. Within a month, the region develops into a quasi-stationary gyre system, which consists of the Southern Gyre near the equator, and the Great Whirl (GW) and Socotra Eddy (SE) to the north. This development has been observed (e.g., Schott et al., 1990) and simulated in models (e.g., Jensen, 1991; Luther & O'Brien, 1985; McCreary & Kundu, 1988). Here we focus on the GW, a large quasi-stationary anticyclonic eddy that forms annually off the coast of Somalia around May and persists throughout the ISM before decaying around December (Düing et al., 1980; Lee et al., 2000).

Depending on the direction of circulation, off-equatorial eddies leave a positive (negative) signature of sea surface height (SSH) in the ocean. Thus, SSH is a very useful diagnostic in identifying and tracking mesoscale eddies since global SSH maps can be delivered daily in near real time by creating composites from the tracks of all altimetric satellites that are simultaneously orbiting. Recent attempts to characterize the GW using SSH have made strides in diagnosing the life cycle of the feature, as well as the local and remote forcing mechanisms, which contribute to high interannual variability in both its timing and intensity. The arrival of annual downwelling Rossby waves at the western boundary from the southern tip of India was pointed out in 1993 by McCreary et al. and later shown to coincide with the formation of the GW through the satellite data of Beal and Donohue (2013). Furthermore, the Findlater Jet reinforces this circulation throughout the duration of the ISM by generating a strong northward flow of the Somali Current along the African coastline. The flow turns offshore along a region of negative wind stress curl to create a coastal wedge of cold, upwelled water (Schott & McCreary, 2001).

The GW plays a crucial role in advecting and mixing upwelled waters generated via alongshore wind stress off the African coastline during the ISM. It is also important in regulating the amount of water from the

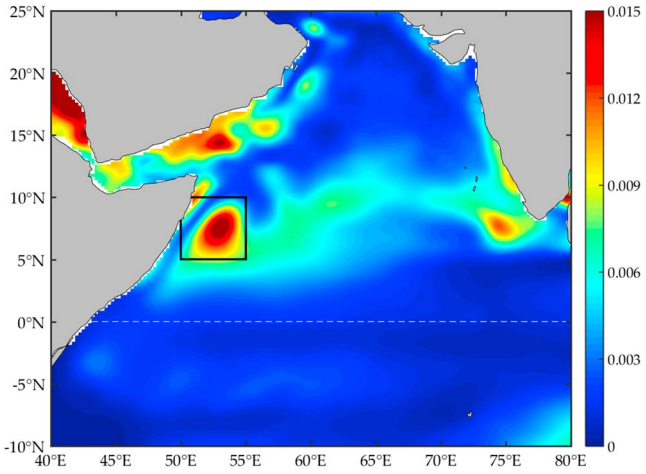

Figure 1. Annual absolute dynamic topography variance (m^2) in the Arabian Sea. The black box indicates the domain used for Great Whirl tracking in this study (5–10°N, 50–55°E).

Southern Hemisphere that penetrates into the interior of the Arabian Sea. The intense Somali Current throughout the boreal summer, reaching a maximum well over 1 m/s during late July (Düing et al., 1980), is thought to be the most important pathway of fresher water into the climatologically salty Arabian Sea (Jensen, 2003). Schott et al. (1997) showed through in situ observations that when the GW is present during the summer, communication between the Somali Current and the interior Arabian Sea is disconnected, save the shallow confines between Socotra and the African mainland. Fischer et al. (1996) later reinforced these observations and estimated that this "Socotra Passage" facilitated an exchange of up to 14 Sv between the Somali Basin and Arabian Sea, a quantity dependent on interactions among the GW and the SE on its northern flank.

Although the GW has been studied comprehensively over a span of several decades, the high-frequency responses to variable wind forcing and internal instabilities at low latitude (Brandt et al., 2003) have made it difficult to accurately isolate phases in the GW life cycle, which could aid forecasting efforts. We believe this is largely due to the challenge of defining the eddy in a consistent manner, as it often does not conform to the behaviors that generally characterize smaller mesoscale eddies. Generic eddy tracking methodologies such as the Okubo-Weiss parameter (Okubo, 1970; Weiss, 1991), vorticity threshold (Benzi et al., 1988; McWilliams, 1990), and streamline geometry (Chaigneau et al., 2008; Sadarjoen & Post, 2000) methods are considered viable options for constraining the GW, but all share limitations that are discussed in section 3.

The close proximity of the eddy to the equator and concurrent monsoon wind stress breaks down the geostrophic approximation that is inherent in SSH-derived velocities, particularly when reliant on double differentiation in generating streamlines. Furthermore, the GW often fluctuates between an open and closed circulation pattern over its lifetime, which would manifest as "disappearing" and "reappearing" in a closed contour analysis as pointed out by Chelton et al. (2011). Thus, studies focused specifically on the GW have often opted to instead define it as an area of SSH exceeding an arbitrary threshold value (Beal & Donohue, 2013) or amplitude (Vic et al., 2014). This study improves the way we constrain the GW by determining various properties through an approach that utilizes a transform to polar coordinates about a proactively assigned center based on local SSH extrema.

2. Data and Methods

Our algorithm defines the GW as follows, utilizing absolute dynamic topography (ADT) as our sea level constraint, since the gyre has a nonnegligible mean dynamic topography relative to its surroundings. The center is first identified as the location of the maximum ADT anomaly in the domain (Figure 1). Piecewise in polar angles (0:2π), azimuths of an ellipse are created that extend outward from this central point. The length of the radius along each azimuth is constrained to a predetermined ADT amplitude relative to the central maximum. The amplitude is a base value of 80%, modified by functions of time and space, making it an independent calculation for each azimuth. A contour enclosing the eddy is then created by connecting the endpoints of remaining azimuths after having flagged and removed those outside of a realistic length scale (limited by the internal Rossby radius of deformation). This flagging procedure allows us to assign a formation and termination date based on the approach of, and departure from, a state of zero flagged azimuths (<5% flags defines eddy). After identifying the GW, each subsequent time step will repeat the routine with the new center location now required to fall within the contour found in the previous time step to ensure consistent tracking. The algorithm operates on the basis of a relative rather than an absolute sea level threshold, which inherently filters out low-frequency variability without requiring additional processing. As it does not necessarily rely on a closed contour to operate, this method poses an advantage for permanent features that behave similarly to mesoscale eddies but lack a permanent closed rotation, such as the GW, Loop Current, and Agulhas retroflection regions. For more details on the algorithm utilized, as well as flagging criteria and validation, see the supporting information.

Gridded sea level maps spanning the years 1993–2015 were obtained from one observational product and one model product for parallel validation of our proposed algorithm. Observational data come from the multimission Level 4 Archiving, Validation, and Interpretation of Satellite Oceanographic data (AVISO) reanalysis product. This data set provides daily satellite-based SSH and ADT observations gridded to a spatial resolution of (1/4)°. Model-derived SSH, as well as ocean u and v current components, were obtained from the HYbrid Coordinate Ocean Model (HYCOM) experiment 53X reanalysis product produced by the U.S. Naval Research Laboratory (Metzger et al., 2017). This general circulation model is forced by the National Centers for Environmental Prediction Climate Forecast System Reanalysis and assimilates observations from satellite, in situ sea surface temperature, and expendable bathythermograph, Argo floats, and moored buoy profiles (Saha et al., 2010). HYCOM includes inertial and Ekman components of surface currents, while AVISO is restricted to geostrophy. Daily HYCOM outputs were retrieved at (1/12)° resolution and remapped in the vertical from isopycnal layers to z levels.

3. Evaluation of GW Tracking Algorithm

The pronounced effect of the ISM on sea level is evident in the annual ADT variance (Figure 1). The separation of the Somali Current from the coastline is seen as a band of low variance extending to the northeast that is surrounded by high variance to the southeast (GW) and northwest (cold wedge). The latitude of this separation throughout the summer monsoon season varies in response to the volume flux of the Somali Current, as is expected given the curvature of the western boundary (Ou & De Ruijter, 1986). The cold wedge characteristic of monsoon-induced upwelling is visible as a region of high variance resembling a continuation of the Somali coast without convex curvature. The GW leaves a signature of high sea level variance over the southwest Arabian Sea centered at 53°E, 8°N, giving us a clear climatological location with which to define our domain (Figure 1).

We establish two criteria to define the size and orientation of an "ideal" GW in order to differentiate various GW identification methods, including our own. First, the enclosing contour should contain a high ratio of negative to positive relative vorticity. Second, the defined perimeter must be in close proximity to the closed contour of maximum current speed.

The method presented in this study is able to more precisely and fully capture the GW's anticyclonic circulation and radius of maximum currents when compared to alternative methods (Figure 2). On average, our algorithm generates a larger surface area than the four alternative methodologies, ensuring the inclusion of the high kinetic energy band along the perimeter of the eddy. The Beal and Donohue (35-cm threshold) contour neglects the weak early stages of the GW (Figure 2a), while the Vic et al. (6-cm amplitude) contour shows minimal temporal evolution and lacks constraints to define formation and termination conditions (Figure 2). Our algorithm is also well suited for interannual studies, where climate oscillations such as the Indian Ocean Dipole shift the background state of the ocean and create difficulty in choosing a single representative threshold value. Moreover, the use of a static geographic domain to study a shifting or expanding feature such as the GW poses a risk of edge damping. Thus, it is advantageous to obtain a specific set of boundaries that are dynamic with respect to time when analyzing the internal dynamics/energetics of the GW, as is true with parametrizations based on the Okubo-Weiss, Chelton, or present study.

Algorithms sharing an underlying concept of closed contour clustering repeatedly underestimated the area of interest, as attempts to sequentially seek the outermost contours often failed to satisfy the closure criterion due to a relatively weak circulation along the southern flank of the gyre. The Chelton et al. (2011) algorithm (largest closed contour about a local extrema) is explicitly shown in Figure 2, but the similar winding angle method developed by Sadarjoen and Post (2000) and refined by Chaigneau et al. (2008) and Trott et al. (2018) was also analyzed, yielding comparable results.

The Okubo-Weiss method is defined here as the $W = -1.5 \times 10^{-12}$ contour, where

$$W = \left(\frac{du}{dx} - \frac{dv}{dy}\right) + \left(\frac{dv}{dx} + \frac{du}{dy}\right) - \left(\frac{dv}{dx} - \frac{du}{dy}\right).$$

This yields the most accurate representation when presented with a relatively homogenous angular flow as in October (Figure 2c). When presented with an irregular shape, the shear component tends to dominate vorticity and thus skews the Okubo-Weiss contour as is true in June (Figure 2a). Irregularities in the

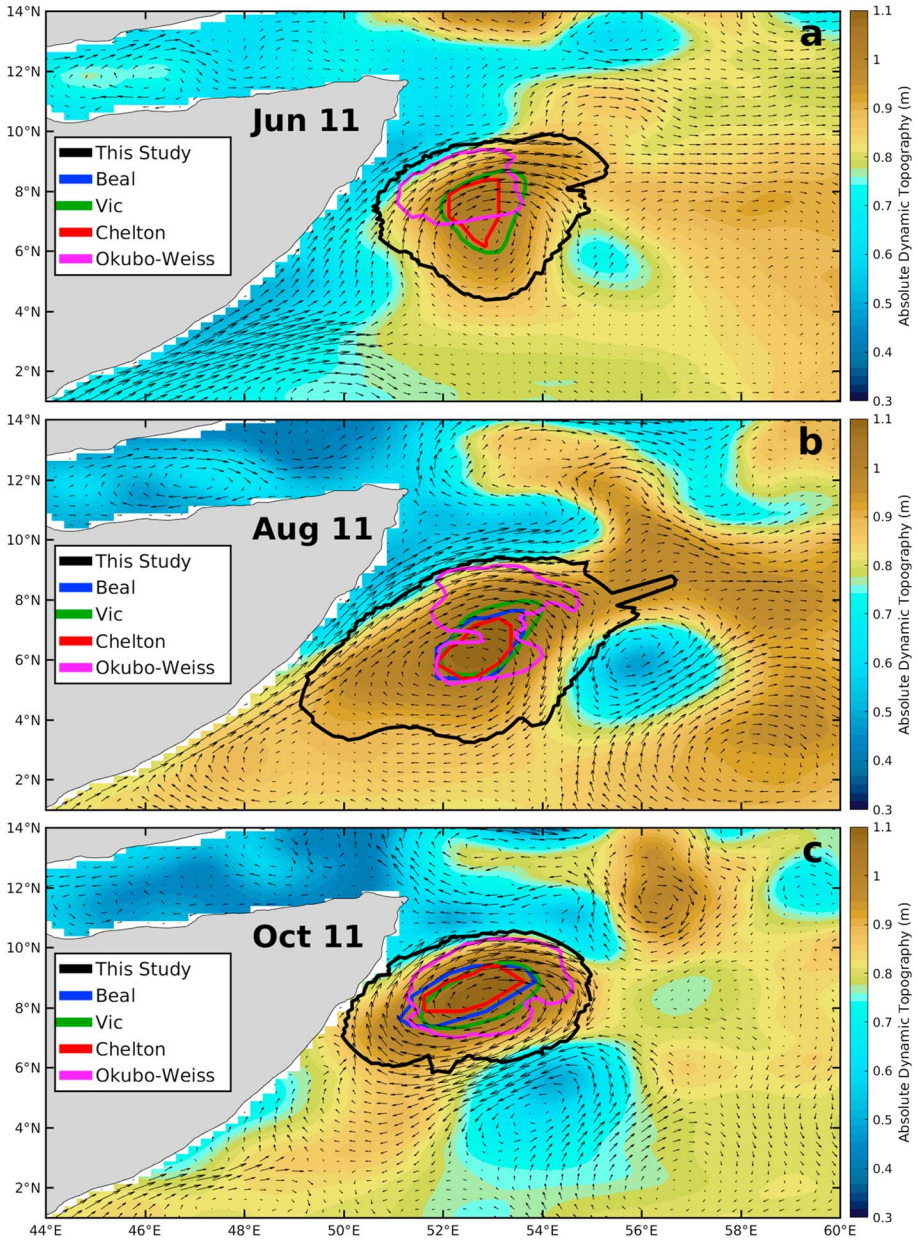

Figure 2. Qualitative results of this study's algorithm in (a) June, (b) August, and (c) October 2012, compared to methods implemented on the Great Whirl in the past. Absolute dynamic topography is shaded, and HYbrid Coordinate Ocean Model surface current vectors are overlayed. Colored contours indicate each method: black = this study; blue = 35-cm sea surface height threshold; green = 6-cm sea surface height amplitude; red = streamline; magenta = -1.5×10^{-12} Okubo-Weiss threshold. The selection of dates coincides with the formation date according to our algorithm (11 June) and subsequent steps at 2-month interval.

shape of the GW arise from friction with the western boundary and intermittent interaction with smaller cyclonic eddies that are shed from the cold wedge and travel around the GW in a clockwise direction. As evidenced in Figure 2, these cyclonic eddies are generated approximately once a month as a dynamical response to internal instability (Jensen, 1991) and effectively compress the shape of the GW along the region of contact. The ability of our algorithm to trace SSH fronts associated with such interactions is important because cyclones can create large vertical mixing through shear stress with one another and are additionally theorized to be a factor in the decay of the GW via injection of positive vorticity (Wirth et al., 2002).

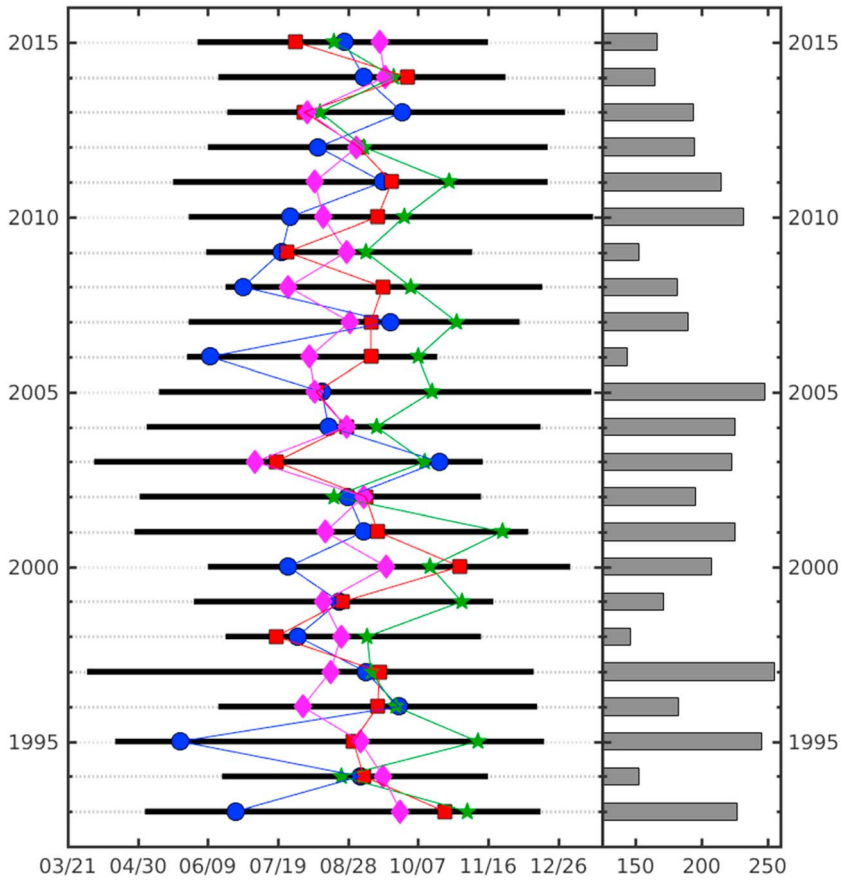

Figure 3. (left) Diagram displaying the date and duration of each Great Whirl event from 1993–2015 (AVISO; solid black lines). The peak dates of surface area (AVISO; blue circles), absolute dynamic topography (AVISO; red squares), 20 °C isotherm depth (HYCOM; green stars), and surface KE (HYCOM; magenta diamonds) are shown. The latter two parameters were spatially averaged over the region enclosed by the GW, while the absolute dynamic topography peak is based on the average amplitude. (right) Duration of each GW event from AVISO, in days. AVISO = Archiving, Validation, and Interpretation of Satellite Oceanographic data; HYCOM = HYbrid Coordinate Ocean Model; GW = Great Whirl.

Despite improvements in enclosing a specific region representative of the GW in near real time, our algorithm has approximately a 2% incidence of overestimated azimuths when presented with low sea level gradients, as seen along the eastern edge of the GW in Figure 2b. Additional constraints (i.e., setting a maximum proximity between adjacent points and retroactive contour smoothing) are planned for future iterations of the algorithm to mitigate such inconsistencies, although they are not applied here.

4. Interannual Variability of the GW Life Cycle

The GW typically forms a couple of weeks prior to the monsoon onset (as defined by Wang et al., 2009), in agreement with studies suggesting an initiation via remote forcing from annual Rossby waves originating at the tip of India (McCreary et al., 1993). Years of anomalously early formation tend to coincide with anomalously late ISM onset and vice versa. On average, the GW has a life span of 198 (170) days based on satellite altimetry (HYCOM reanalysis) data (Figure 3). On average, this is longer than previous life span estimates derived from surface measurements (166 days [Beal & Donohue, 2013]; 140 days [Trott et al., 2018]), albeit consistent with bathythermograph observations that revealed a subsurface persistence of anticyclonic circulation extending into the following calendar year (Bruce et al., 1981). Indeed, our analysis noted three occasions (2000, 2005, and 2010) in which the GW was present the following year, although it never persisted beyond January. A comparison to climate indices implies that long (short) GW and ISM life spans coincide with La Niña (El Niño) onset during years when the Indian Ocean Dipole is weak (see also

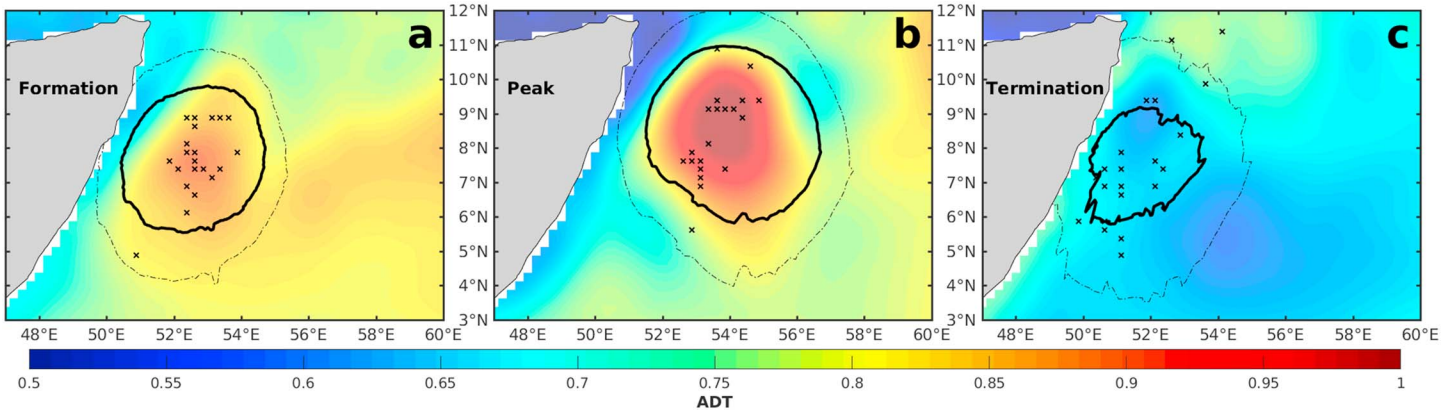

Figure 4. Composite of ADT in the southwest Arabian Sea at the (a) formation, (b) maximum sea surface height, and (c) termination date of the GW for the 1993–2015 period. The solid black line is a composite of the enclosing contour of the GW, and the dashed line is +1 standard deviation outward from the solid contour. The scatter points correspond to the location of the geometric center of the GW for each year sampled. ADT = absolute dynamic topography; GW = Great Whirl.

Xavier et al., 2007). Additional decomposition based on geospatial "flavors" of El Niño–Southern Oscillation (ENSO; Text S2) reveals preferences that are seemingly independent of the ENSO phase. On average, the GW life span is 41 days longer during Central Pacific ENSO events and 32 days shorter during Eastern Pacific ENSO events (Figure S4). In addition, very long events tend to be followed by very short events, particularly during the '93/'94, '95/'96, and '05/'06 seasons. The kinetic energy peak date shows a similar alternating pattern, although the relative timing of this peak consistently falls around the midpoint of the full life cycle (52% on average; Figure 3, diamonds), earlier than that found by Trott et al. (2018). Of the four variables analyzed, the surface area (Figure 3, circles) tended to peak the earliest (43% of events), followed by an intensification and deepening of the eddy from July–September. The inertia generated during the monsoon helps the GW to maintain its rotation after direct forcing starts to diminish, which manifests as an increase in the depth-to-surface area ratio following maximum vertical extent in early October (Figure 3, stars).

On average, the GW forms near 53°E, 8°N and shifts about 100 km east by the time it reaches maximum intensity (Figure 4). The location of the GW upon termination displays much greater interannual variability, with 750 km separating the termination point of the southern interannual extreme (2002) from the northern interannual extreme (2000). The results of previous observational studies (Beal & Donohue, 2013; Bruce & Beatty, 1985) suggest a southward migration and coalescence with the southern gyre during the decay phase, while the results of modeling efforts (Vic et al., 2014) suggest a northward migration and coalescence with the SE. Additionally, Wirth et al. (2002) suggested that the GW may split into two anticyclonic eddies during the month of October. Our results, in tracking the GW generated during the ISM, indicate a southward migration in the final month during 50% of the years studied (Figure 4c).

Furthermore, in instances where this southward migration is observed, the SE generally exhibits a clockwise orbit of the island before detaching at the southern tip of Socotra and likewise migrating south. Thus, the subsurface circulation at 10°N observed by Bruce et al. (1981) during the subsequent northeast monsoon season is likely a signature of SE origin rather than GW origin. All instances of northward GW migration resulted in coalescence with the SE, occurring in five of the 23 years studied (1997, 2000, 2001, 2005, and 2010). The distribution of locations at the peak of the GW (Figure 4b) resembles two distinct clusters; one cluster near 53°E, 7.5°N and one cluster near 53°E, 9°N. This implies some degree of predictability as to the pattern of decay that is to be expected in the months following, as the northern cluster generally continues north and the southern cluster generally continues south.

With regard to the typical life of a GW event, the surface area, surface magnitude, and depth all plateau in early September and decay more rapidly than the growth stage during the summer season (Figures 5a–5c). The close resemblance of sea level and isotherm depth curves is an encouraging sign that the surface signature of the GW is representative of the underlying homogenous layer to depths of up to 100 m. The average peak value of surface area corresponds to an equivalent radius of 309 km. Absolute KE from HYCOM is on

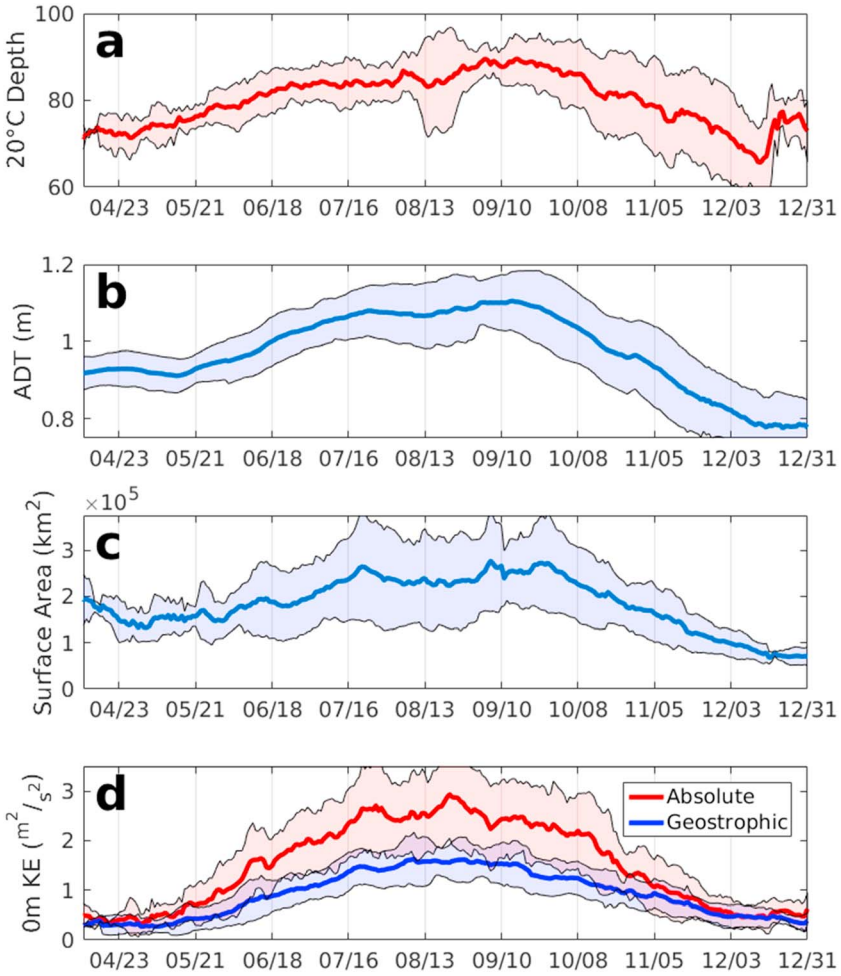

Figure 5. Time series of (a) 20 °C isotherm depth averaged within the GW, (b) absolute dynamic topography at GW center, (c) surface area, and (d) surface kinetic energy averaged along the GW perimeter. Blue lines indicate values calculated from Archiving, Validation, and Interpretation of Satellite Oceanographic data altimetry, while red lines indicate values calculated from HYbrid Coordinate Ocean Model surface currents. All shaded regions indicate ±2 standard deviations. GW = Great Whirl; ADT = absolute dynamic topography.

average 55% greater than geostrophic KE from AVISO when the GW is present, supporting the findings of field observations from Beal and Donohue (2013) that estimated a 60–70% underestimation of geostrophic velocities relative to acoustic Doppler current profiler measurements (Figure 5d). The two lines converge near the formation and termination dates of the GW, revealing a diminished discrepancy during the intermonsoon periods when direct forcing is weak.

5. Conclusions

A novel algorithm for identification and tracking of the GW is presented, which provides a more case-specific approach than traditional mesoscale eddy tracking algorithms that can be implemented in near real time. An examination of 22 years of general circulation model reanalysis data and 23 years of satellite altimetry reveals the broad interannual range of both timing and duration of the GW. Observations of GW onset prior to ISM onset support the suggested formation mechanism of vorticity injection via first and second baroclinic mode Rossby waves as proposed by former observational (Brandt et al., 2003) and model studies (McCreary et al., 1993). The large ageostrophic component of circulation during the mature phase highlights the discretion that must be exercised when making inferences based on geostrophic approximations of near-surface ocean currents during the summer monsoon. Despite an average migration of 4,100 km over the course of one life span, the net displacement from formation to termination averages just 280 km. The

factors determining migration and subsurface dynamics during the decay phase remains a topic of interest, as artifacts of the eddy are shown to persist into the winter monsoon season.

Acknowledgments
AVISO data can be accessed at http://marine.copernicus.eu/. HYCOM Reanalysis is stored at the Navy DoD Supercomputing Resource Center (DSRC). Access to the DSRC may be obtained through a request to the DoD High Performance Computer Modernization Program (https://www.hpc.mil/). This study was supported by the U.S. Office of Naval Research NASCar (73-4347-34-5) project and the Naval Research Laboratory Karle's Fellowship. We thank Abhisek Chatterjee and an anonymous reviewer for their valuable feedback that significantly improved the manuscript and also Ebenezer Nyadjro for his contributions in developing the methodology utilized in this manuscript.

References

Beal, L., & Donohue, K. (2013). The Great Whirl: Observations of its seasonal development and interannual variability. *Journal of Geophysical Research: Oceans*, *118*, 1–13. https://doi.org/10.1029/2012JC008198

Benzi, R., Patarnello, S., & Santangelo, P. (1988). Self-similar coherent structures in two-dimensional decaying turbulence. *Journal of Physics A: Mathematical and General*, *21*(5), 1221–1237. https://doi.org/10.1088/0305-4470/21/5/018

Brandt, P., Dengler, M., Rubino, A., Quadfasel, D., & Schott, F. (2003). Intraseasonal variability in the southwestern Arabian Sea and its relation to the seasonal circulation. *Deep-Sea Research*, *50*(12-13), 2129–2141. https://doi.org/10.1016/S0967-0645(03)00049-3

Bruce, J. G., & Beatty, W. H. (1985). Some observations of the coalescing of Somali eddies and a description of the Socotra eddy. *Oceanologica Acta*, *8*(2), 207–219.

Bruce, J. G., Fieux, M., & Gonella, J. (1981). A note on the continuance of the Somali eddy after the cessation of the southwest monsoon. *Oceanologica Acta*, *4*(1), 7–9.

Chaigneau, A., Gizolme, A., & Grados, C. (2008). Mesoscale eddies off Peru in altimeter records: Identification algorithms and eddy spatio-temporal patterns. *Progress in Oceanography*, *79*(2–4), 106–119. https://doi.org/10.1016/j.pocean.2008.10.013

Chelton, D. B., Schlax, M. G., & Samelson, R. M. (2011). Global observations of nonlinear mesoscale eddies. *Progress in Oceanography*, *91*(2), 167–216. https://doi.org/10.1016/j.pocean.2011.01.002

Düing, W., Molinari, R., & Swallow, J. (1980). Somali Current: Evolution of surface flow. *Science*, *209*(4456), 588–590. https://doi.org/10.1126/science.209.4456.588-a

Fischer, J., Schott, F., & Stramma, L. (1996). Currents and transports of the Great Whirl-Socotra gyre system during the summer monsoon, August 1993. *Journal of Geophysical Research*, *101*(C2), 3573–3587. https://doi.org/10.1029/95JC03617

Jensen, T. G. (1991). Modeling the seasonal undercurrents in the Somali Current system. *Journal of Geophysical Research*, *96*(C12), 22,151–22,167. https://doi.org/10.1029/91JC02383

Jensen, T. G. (2003). Cross-equatorial pathways of salt and tracers from the northern Indian Ocean: Modelling results. *Deep-Sea Research*, *50*(12-13), 2111–2127. https://doi.org/10.1016/S0967-0645(03)00048-1

Lee, C., Jones, B., Brink, K., & Fischer, A. (2000). The upper-ocean response to monsoonal forcing in the Arabian Sea: Seasonal and spatial variability. *Deep Sea Research, Part II*, *47*(7-8), 1177–1226. https://doi.org/10.1016/S0967-0645(99)00141-1

Luther, M. E., & O'Brien, J. J. (1985). A model of the seasonal circulation in the Arabian Sea forced by observed winds. *Progress in Oceanography*, *14*, 353–385. https://doi.org/10.1016/0079-6611(85)90017-5

McCreary, J. P., & Kundu, P. K. (1988). A numerical investigation of the Somali Current during the southwest monsoon. *Journal of Marine Research*, *46*(1), 25–58. https://doi.org/10.1357/002224088785113711

McCreary, J. P., Kundu, P. K., & Molinari, R. (1993). A numerical investigation of dynamics, thermodynamics and mixed-layer processes in the Indian Ocean. *Progress in Oceanography*, *31*(3), 181–244. https://doi.org/10.1016/0079-6611(93)90002-U

McWilliams, J. C. (1990). The vortices of two-dimensional turbulence. *Journal of Fluid Mechanics*, *219*(1), 361–385. https://doi.org/10.1017/S0022112090002981

Metzger, E. J., Helber, R. W., Hogan, P. J., Posey, P. G., Thoppil, P. G., Townsend, T L., et al. (2017). Global Ocean Forecast System 3.1 validation testing. Naval Research Laboratory Technical Report. Retrieved from http://www.dtic.mil/docs/citations/AD1034517

Okubo, A. (1970). Horizontal dispersion of floatable particles in the vicinity of velocity singularities such as convergences. *Deep Sea Research*, *17*, 445–454.

Ou, H. W., & De Ruijter, W. P. (1986). Separation of an inertial boundary current from a curved coastline. *Journal of Physical Oceanography*, *16*(2), 280–289. https://doi.org/10.1175/1520-0485(1986)016<0280:SOAIBC>2.0.CO;2

Sadarjoen, I. A., & Post, F. H. (2000). Detection, quantification, and tracking of vortices using streamline geometry. *Computers & Graphics*, *24*(3), 333–341. https://doi.org/10.1016/S0097-8493(00)00029-7

Saha, S., Moorthi, S., Pan, H. L., Wu, X., Wang, J., Nadiga, S., et al. (2010). The NCEP climate forecast system reanalysis. *Bulletin of the American Meteorological Society*, *91*(8), 1015–1058. https://doi.org/10.1175/2010BAMS3001.1

Schott, F., Fischer, J., Garternicht, U., & Quadfasel, D. (1997). Summer monsoon response of the northern Somali Current. *Geophysical Research Letters*, *24*(21), 2565–2568. https://doi.org/10.1029/97GL00888

Schott, F., & McCreary, J. P. Jr. (2001). The monsoon circulation of the Indian Ocean. *Progress in Oceanography*, *51*(1), 1–123. https://doi.org/10.1016/S0079-6611(01)00083-0

Schott, F., Swallow, J. C., & Fieux, M. (1990). The Somali Current at the equator: Annual cycle of currents and transports in the upper 1000 m and connection to neighbouring latitudes. *Deep Sea Research Part A. Oceanographic Research Papers*, *37*(12), 1825–1848. https://doi.org/10.1016/0198-0149(90)90080-F

Trott, C. B., Subrahmanyam, B., Chaigneau, A., & Delcroix, T. (2018). Eddy tracking in the northwestern Indian Ocean during southwest monsoon regimes. *Geophysical Research Letters*, *45*, 6594–6603. https://doi.org/10.1029/2018GL078381

Vic, C., Roullet, G., Carton, X., & Capet, X. (2014). Mesoscale dynamics in the Arabian Sea and a focus on the Great Whirl life cycle: A numerical investigation using ROMS. *Journal of Geophysical Research: Oceans*, *119*, 6422–6443. https://doi.org/10.1002/2014JC009857

Wang, B., Ding, Q., & Joseph, P. V. (2009). Objective definition of the Indian Summer Monsoon Onset. *Journal of Climate*, *22*(12), 3303–3316. https://doi.org/10.1175/2008JCLI2675.1

Weiss, J. (1991). The dynamics of enstrophy transfer in two-dimensional hydrodynamics. *Physica D: Nonlinear Phenomena*, *48*(2–3), 273–294. https://doi.org/10.1016/0167-2789(91)90088-Q

Wirth, A., Willebrand, J., & Schott, F. (2002). Variability of the Great Whirl from observations and models. *Deep Sea Res. Part II: Tropical Studies in Oceanography*, *49*(7–8), 1279–1295. https://doi.org/10.1016/S0967-0645(01)00165-5

Xavier, P. K., Marzin, C., & Goswami, B. N. (2007). An objective definition of the Indian summer monsoon season and a new perspective on the ENSO–monsoon relationship. *Quarterly Journal of the Royal Meteorological Society*, *133*(624), 749–764. https://doi.org/10.1002/qj.45